RSC Advances

ROYAL SOCIETY OF CHEMISTRY

PAPER

View Article Online
View Journal | View Issue

Cite this: *RSC Adv.*, 2025, **15**, 43377

Judd–Ofelt analysis and the spectroscopic elucidation of β-BaB_2O_4:Eu^{3+} phosphors for optoelectronic applications

R. Kiran,†[a] Vaishnavi Shenoy,†[a] M. I. Sayyed,[bcd] Aljawhara H. Almuqrin[e] and Sudha D. Kamath *[a]

Received 7th August 2025
Accepted 1st November 2025

DOI: 10.1039/d5ra05778g

rsc.li/rsc-advances

We have used the solid-state reaction method to prepare Eu^{3+} (1, 1.5, 2, 2.5, and 3 mol%) doped β-BaB_2O_4 phosphors. Phase purity of the prepared phosphors was confirmed using X-ray diffraction (XRD) studies. Photoluminescence (PL) measurements using 395 nm excitation exhibited three intense peaks at 593 nm, 615 nm, 653 nm, and 702 nm, respectively, due to the $^5D_0 \rightarrow {}^7F_j$ ($j = 0$, 1, and 2) transitions. The PL emission intensity will increase up to 2 mol%, and thereafter, there will be a decline due to concentration quenching. Chromaticity analysis, along with correlated colour temperature (1796 K to 1976 K), confirmed the material's potential as a warm light emitter. Diffuse reflectance spectroscopy revealed a direct bandgap energy of 4.30 eV for the optimized sample. Finally, using Judd–Ofelt intensity parameters, the calculation of critical radiative parameters, including transition probability, lifetime, and branching ratio, was carried out. The results demonstrate the efficient luminescence and excellent colour stability of β-BaB_2O_4:Eu^{3+}, highlighting its potential for optoelectronic applications.

1 Introduction

In the span of the past century, advances in materials science have transformed technologies from silicon-based electronics and lightweight composites to high-performance polymers, reshaping various aspects of life.[1–4] These innovations have enabled faster computing, sustainable energy solutions, fundamentally altering how we live and interact with the world.[5–7] Among the various novel materials, phosphors doped with rare-earth (RE) elements have revolutionized lighting and display technologies by converting ultraviolet or blue excitation into vibrant visible emissions. From energy-efficient fluorescent lamps and high-definition plasma screens to advanced bioimaging probes, phosphors have enabled more sustainable and more versatile applications that touch virtually every aspect of modern life.[8–11] Among the various phosphors, RE-doped borate phosphors have emerged as highly attractive materials, owing to their robust physicochemical stability, broad vacuum-ultraviolet transparency, and elevated resistance to photodamage. The flexible crystal lattices of the borate group readily incorporate a variety of RE activator ions, which enables the fine-tuning of emission properties. Furthermore, the emissive behaviour of these phosphors is known to be sensitive to parameters such as synthesis route, particle size and morphology, host lattice symmetry, and activator site occupancy. Such tunability makes RE borate phosphors an ideal candidate for plasma display panels, mercury-free fluorescent lamps, and next-generation solid-state lighting devices.[12–14]

In the present study, β-BaB_2O_4 was selected as the host matrix for phosphor development and doped with varying concentrations of RE ions. Previous investigations involving this host have demonstrated its suitability for luminescent applications, including systems such as β-BaB_2O_4:Dy^{3+},[15] β-BaB_2O_4:Sm^{3+},[16] β-BaB_2O_4:Nd^{3+}, Yb^{3+},[17] and β-BaB_2O_4:Pb^{2+}, Cu^{2+}.[18] In this work, Eu^{3+} was selected as the activator due to its high chemical reactivity and stable trivalent oxidation state under ambient conditions. The Eu^{3+} ion exhibits sharp emissions due to the $^5D_0 \rightarrow {}^7F_J$ ($J = 0$, 1, 2, 3, 4, 5, 6) electronic transitions, making it highly suitable for red luminescence.[19] As a result, Eu^{3+} activated phosphors are considered to be a promising contender for efficient red spectral component in white light-emitting diode (WLED) technologies.[20–23] Prior studies by Jie Liu *et al.* and Zhihua Li *et al.* have mainly focused on the room temperature optical properties of Eu^{3+} doped β-BaB_2O_4 phosphors. Jie Liu *et al.* synthesized β-BaB_2O_4:xEu^{3+} ($x = 0.00$, 0.02, 0.04, 0.06, 0.08, 0.10) phosphors and evaluated the impact of various charge compensating ions (K^+, Na^+, and Li^+) on PL emission intensity.[24] Their findings indicated that

[a]*Department of Physics, Manipal Institute of Technology, Manipal Academy of Higher Education, Manipal, Karnataka, India. E-mail: sudha.kamath@manipal.edu*

[b]*Renewable Energy and Environmental Technology Center, University of Tabuk, Tabuk, 47913, Saudi Arabia*

[c]*Department of Physics, Faculty of Science, Isra University, Amman, Jordan*

[d]*Department of Physics and Technical Sciences, Western Caspian University, Baku, Azerbaijan*

[e]*Department of Physics, College of Science, Princess Nourah Bint Abdulrahman University, P.O. Box 84428, Riyadh, 11671, Saudi Arabia*

† These authors contributed equally to this work.

incorporating charge compensators enhanced PL intensity, with K^+ yielding the most significant improvement. However, this study did not include a comprehensive analysis of the crystal structure *via* XRD, the reflectance measurements, and the thermal stability. In another effort, Zhihua Li *et al.* synthesized BaB_2O_4:Eu^{3+} phosphors and explored similar optical properties.[25] Nonetheless, the reported XRD data exhibited high background noise and secondary phase peaks, suggesting the presence of impurities. Additionally, the selected dopant concentrations (5.69, 7.48, 10.30, 12.00, 16.10, 18.90, 20.60, and 21.30 mol%) deviate drastically from the range reported by Jie Liu *et al.*, and the study lacked both reflectance analysis and the stability of the phosphor under elevated temperature conditions. Also, none of the reported studies carried out Judd–Ofelt (JO) analysis and the evaluation of the radiative parameters.

Therefore, in the present investigation, β-BaB_2O_4:xEu^{3+} (x = 1, 1.5, 2, 2.5, and 3 mol%) phosphors were prepared *via* the solid-state reaction method. This work aims to bridge existing research gaps by offering a systematic and comprehensive investigation of the material's optical, reflectance, colour tunability, structural properties, and thermal stability. In addition, using the JO theory, radiative parameters were evaluated for the prepared phosphors to check their suitability for various optoelectronic applications.

2 Experimental

2.1 Phosphor synthesis

We have prepared β-BaB_2O_4:Eu^{3+} phosphors *via* the solid-state reaction method. Initially, precisely weighted $BaCO_3$ (99%), H_3BO_3 (99%), and Eu_2O_3 (99.99%) are taken in stoichiometric amounts and carefully ground to ensure uniform distribution and improved homogeneity throughout the mixture. Following this, the resulting mixtures were transferred to an alumina crucible and calcinated at 800 °C for three hours. Finally, the samples were cooled to room temperature and readied for further characterization.

2.2 Material analysis techniques

Crystal structure and the phase purity of the synthesized phosphors were verified through XRD analysis, conducted over a 2θ range of 15–70° using a Rigaku Miniflex 600 diffractometer. PL excitation and emission spectra were subsequently recorded using a JASCO FP-800 spectrofluorometer. Optical reflectance and absorption spectra were evaluated *via* the diffuse reflectance spectroscopy (DRS) mode with the help of a PerkinElmer Lambda 900 spectrophotometer. Finally, the thermal stability of the sample was assessed through thermogravimetric analysis (TGA) using a PerkinElmer TGA 4000, with measurements conducted up to 500 °C.

3 Results and discussion

3.1 Analysis of phosphor structure

XRD analysis confirmed the crystalline phase of the β-BaB_2O_4:Eu^{3+} phosphors. As shown in Fig. 1, the diffraction pattern exhibits peak positions that are well-aligned with those of the standard reference (JCPDS card no. 80-1049) patterns, indicating the successful formation of pure β-BaB_2O_4:Eu^{3+} phase. The absence of secondary or impurity peaks suggests that the incorporation of Eu^{3+} ions has a negligible impact on the structure of the host crystal lattice. A closer examination of the XRD pattern between 24° and 27° in Fig. 1 shows that, at 1.5 mol% Eu^{3+} doping, the XRD peaks shift slightly toward higher 2θ values. This behaviour can be attributed to the substitution of larger Ba^{2+} ions by smaller Eu^{3+} ions, leading to a contraction of the unit cell.[26] Interestingly, at higher doping concentrations of 2.5 mol% and 3.0 mol% Eu^{3+}, the peaks shift toward lower 2θ values. This anomalous behaviour suggests that, beyond a certain concentration, Eu^{3+} ions preferentially occupy interstitial sites rather than substituting Ba^{2+} ions. Occupation of interstitial sites expands the interplanar spacing and increases the unit cell volume, resulting in the observed shift of diffraction peaks to lower angles.[27]

This can be understood using the acceptable percentage difference (R_a) between the host and dopant ions should generally remain below 30% to ensure successful substitution without significant lattice distortion.[28] It can be evaluated through the expression given below[29]

$$R_a = \frac{|R_h(CN) - R_{Eu}(CN)|}{R_h(CN)} \quad (1)$$

Here, R_h represents the ionic radius of the host cations, R_{Eu} is that of the Eu^{3+} ion, and CN stands for the coordination number. The values were calculated based on Shannon ionic radius data, with the outcomes presented in Fig. 2(a). As shown, the estimated R_a value for the Eu^{3+}–Ba^{2+} ion pair falls within the permissible threshold, indicating a compatible ionic size match. Therefore, Eu^{3+} ions will successfully substitute Ba^{2+} sites within the host lattice without causing significant structural distortion. Additionally, we have drawn the visual representation of the unit using the reference file, and it is provided as Fig. 2(b).

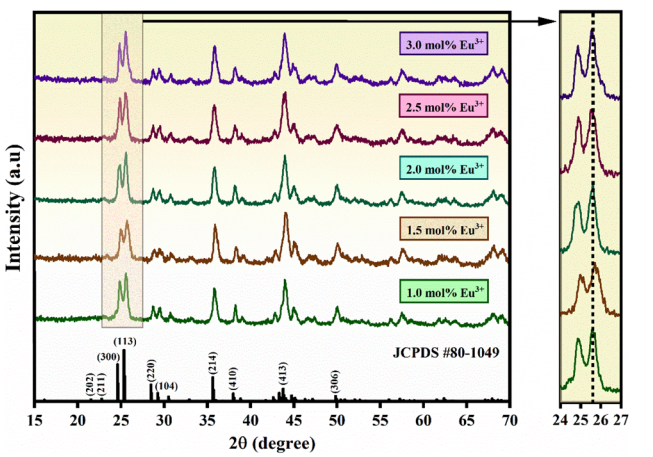

Fig. 1 Experimental XRD patterns overlaid with standard reference peaks confirming the crystalline phase of the phosphors.

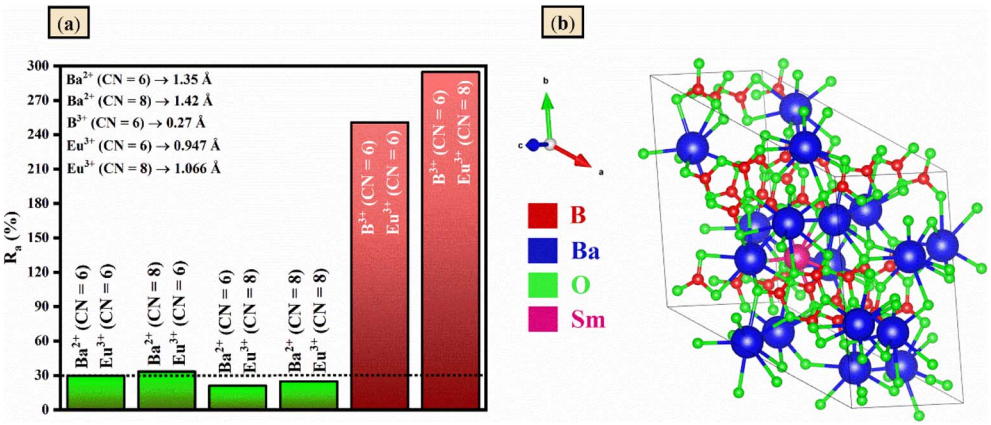

Fig. 2 (a) Acceptable percentage difference in radii (b) pictorial representation of the unit cell.

Subsequently, the crystallite size (D) of the synthesized phosphor was estimated using the Size–Strain Plot (SSP) method. In this approach, it is proposed that the broadening due to the crystallite size follows a Lorentzian distribution, while the strain-induced broadening by a Gaussian function. Based on these assumptions, the following relationship was applied[30]

$$(\beta d \cos\theta)^2 = \frac{0.9\lambda}{D}(\beta d^2 \cos\theta) + \left(\frac{\varepsilon}{2}\right)^2 \quad (2)$$

In this equation, λ denotes the wavelength of the X-ray, β refers to the FWHM of the peak, and d indicates the spacing between lattice planes. To evaluate the crystallite size, a plot of $(\beta d \cos\theta)^2$ *versus* $(\beta d^2 \cos\theta)$ was constructed for all major diffraction peaks for β-BaB_2O_4:xEu^{3+} (x = 1, 1.5, 2, 2.5, and 3 mol%) phosphors, and it is shown in Fig. 3(a)–(e). From the linear fit of each dataset, the crystallite sizes were calculated using the slope of the fitted line. The estimated crystallite sizes were found to be 14.4 nm, 11.6 nm, 14.4 nm, 16.1 nm, and 16.1 nm, respectively, when the concentration of Eu^{3+} varies from 1 mol% to 3 mol%.

3.2 Phosphor optimization and analysis of PL properties

To comprehensively understand the optical characteristics of the phosphors, the excitation spectrum was recorded at room temperature. The PL excitation spectrum corresponding to 2 mol% Eu^{3+} is illustrated in Fig. 4 using an emission wavelength at 615 nm across the 240–500 nm wavelength range. The spectrum reveals key insights into the electronic transitions involved in the luminescence mechanism. A prominent broad excitation band is observed in the 240 to 290 nm region, which is attributed to the charge transfer band (CTB) associated with the Eu^{3+} ions. This CTB originates from an electron transition between the 2p orbital of the oxygen anion to the partially filled 4f orbitals of the Eu^{3+} ion.

This type of transition is characteristic of RE-doped oxide materials, and its presence indicates strong covalent interactions between the host lattice and the dopant ion.[31] In addition to the CTB, sharp excitation peaks are detected in the 295–480 nm range, signifying the intra-4f transitions. These peaks are observed at 299, 321, 363, 384, 395, 416, and 467 nm, corresponding to the intra-4f transitions from the ground state ($^7F_0$) to the excited states ($^5F_4$, $^5H_6$, $^5L_8$, $^5L_7$, $^5L_6$, $^5D_3$, and $^5D_2$).[32] Although f–f electronic transitions are generally forbidden by parity selection rules, the local asymmetry of the crystal field surrounding the Eu^{3+} ions relaxes these restrictions.[33] Among the observed excitation peaks, the one centered at 395 nm displayed the strongest intensity and was consequently selected as the optimal excitation wavelength.

As illustrated in Fig. 5, the emission spectra display multiple sharp and well-defined peaks in the 550–750 nm wavelength range, characteristic of Eu^{3+} transitions. These peaks originate from the intra-configurational f–f transitions of Eu^{3+} ions, specifically from the excited $^5D_0$ level to the various sublevels of the ^7F_J ground state (J = 0–4). Among these transitions, the most intense emission, centered around 615 nm ($^5D_0 \rightarrow {}^7F_2$), corresponds to the $^5D_0 \rightarrow {}^7F_2$ transition. Additional emission bands are observed at approximately 581 nm ($^5D_0 \rightarrow {}^7F_0$), 593 nm ($^5D_0 \rightarrow {}^7F_1$), 653 nm ($^5D_0 \rightarrow {}^7F_3$), and 702 nm ($^5D_0 \rightarrow {}^7F_4$), respectively.[34] Fig. 6 illustrates the simplified energy transfer pathway from $O^{2-} \rightarrow Eu^{3+}$ along with the detailed emission mechanism of Eu^{3+} ions. The corresponding intensity variations of the emission peaks at 593, 615, and 702 nm are presented in Fig. 7(a).[35–37]

Notably, the $^5D_0 \rightarrow {}^7F_2$ transition is an electric dipole (ΔJ = 2) transition, often termed a hypersensitive transition due to its pronounced sensitivity to the local crystal field surrounding Eu^{3+} ions. In contrast, the $^5D_0 \rightarrow {}^7F_1$ transition, identified as a magnetic dipole transition, is relatively insensitive to variations in the local crystal field environment. Based on JO theory, such dominant electric dipole transition suggests that Eu^{3+} ions are situated at non-centrosymmetric sites within the host lattice. In non-centrosymmetric environments, the electric dipole transitions become parity-allowed, particularly evident in the 610–630 nm emission range, while magnetic dipole transitions are parity-forbidden. Conversely, if Eu^{3+} ions are situated at the inversion symmetry sites, the magnetic dipole transitions prevail due to the suppression of the electric dipole pathway.[38] To quantitatively evaluate the local site symmetry of Eu^{3+}, the

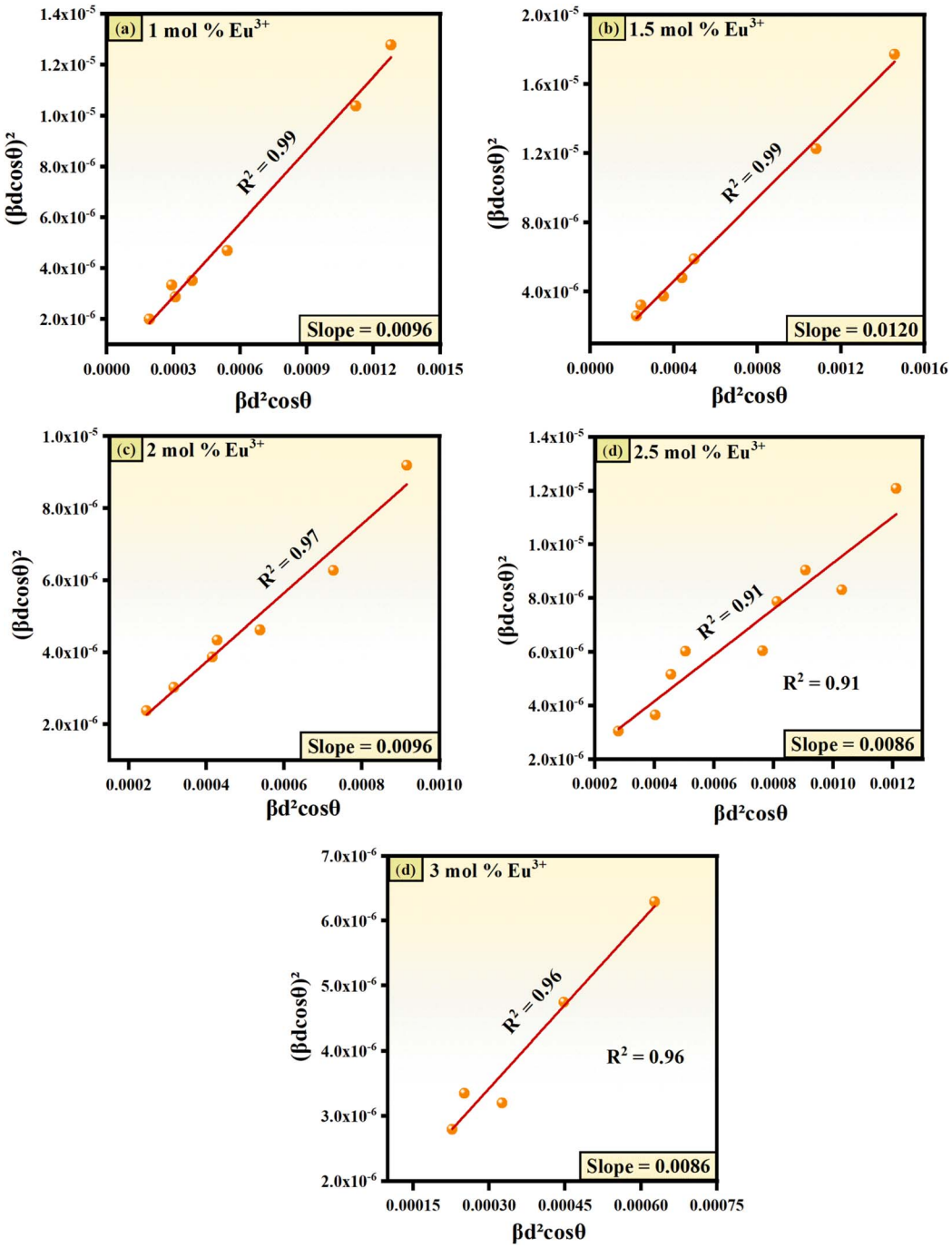

Fig. 3 (a)–(e) SSP plot for the phosphor with dopant concentration.

asymmetry ratio, defined as I_{ED}/I_{MD}, was determined.[39] Values of this ratio are provided in Fig. 7(b), and it ranges between 1.18 and 1.74, indicating a significant degree of local asymmetry around the Eu^{3+} ion, corroborating its incorporation into non-centrosymmetric positions within the host structure.[40] Notably, the emission intensity increases steadily with higher Eu^{3+} doping levels, reaching a maximum at $x = 2$ mol%. Above this concentration, the intensity diminishes due to the concentration quenching. This is due to the enhanced non-radiative energy transfer among neighboring Eu^{3+} ions, which leads to diminished radiative recombination efficiency.

To better understand the nature of the interaction mechanism at higher Eu^{3+} concentrations, the critical distance (R_c) is computed. It represents the average distance at which non-radiative energy transfer becomes significant, and the following relation is employed to compute R_c[41]

$$R_c = 2\left[\frac{3V}{4\pi x_c N}\right]^{1/3} \quad (3)$$

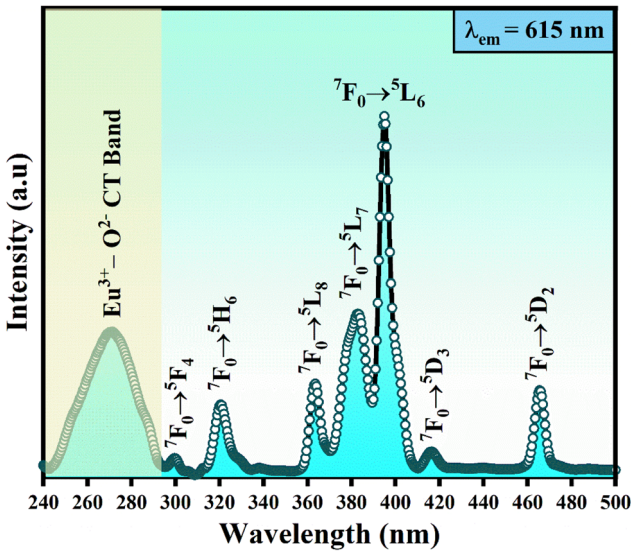

Fig. 4 Excitation spectrum corresponding to the β-BaB_2O_4:xEu^{3+} (x = 2 mol%) phosphors.

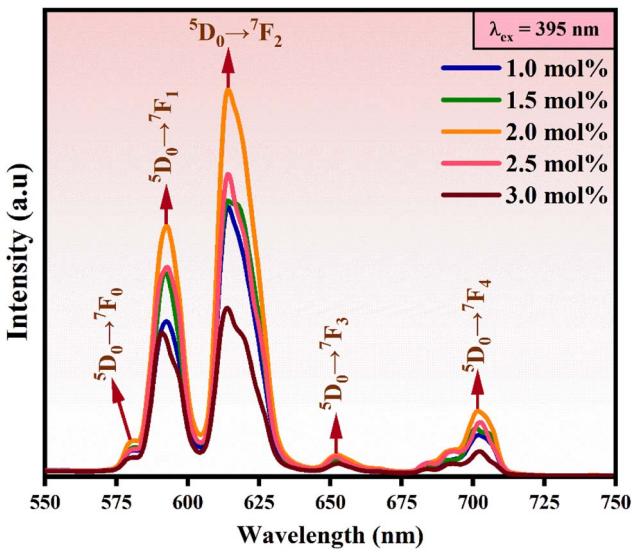

Fig. 5 PL emission spectra for β-BaB_2O_4:xEu^{3+} with excitation at 395 nm.

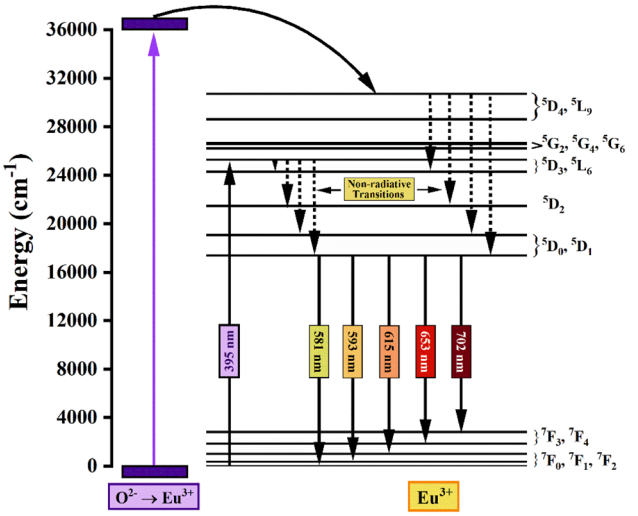

Fig. 6 Energy level diagram of Eu^{3+} describing various emission peaks.

In this equation, V and N represent the volume of the unit cell and the number of available cationic sites per unit cell that can be substituted by Eu^{3+} ions. Furthermore, x_c denotes the optimum dopant concentration. The R_c value was found to be approximately 23.96 Å, and according to theoretical models, when R_c > 5 Å, the dominant quenching mechanism is attributed to multipole–multipole interactions rather than short-range exchange interaction.[42] Thus, the concentration quenching observed is mainly attributed to long-range multipolar interactions between Eu^{3+} ions.

From Dexter's theory, the emission intensity (I) of each Eu^{3+} ion in a luminescent material can be described as a function dependent on dopant concentration (x) using the following equation[43,44]

$$\frac{I}{x} = K\left\{1 + \beta x^{\frac{Q}{3}}\right\}^{-1} \quad (4)$$

In this expression, β and K are the numerical constants influenced by the host β-BaB_2O_4 as well as the excitation parameters. The parameter Q characterizes the nature of the non-radiative interaction mechanism between neighbouring Eu^{3+} ions. The value of Q may be 6, 8, or 10, corresponding respectively to dipole–dipole, dipole–quadrupole, and quadrupole–quadrupole interactions.[45] Under the assumption that $\beta x^{Q/3} \gg 1$, we get

$$\log_e \frac{I}{x} = -\frac{Q}{3}\log_e(x) + \text{constant} \quad (5)$$

To determine the precise value of the interaction parameter Q, a plot of $\log_e \frac{I}{x}$ *versus* $\log_e(x)$ is presented in Fig. 8, the linear graph has a slope of −2.08, which is associated with a Q value of 6.24. This result is closely aligned with $Q = 6$, and hence the concentration quenching of Eu^{3+} luminescence primarily arises from dipole–dipole energy transfer interactions in the investigated host material.

Furthermore, the decay profiles of the Eu^{3+} doped phosphors were well fitted using a mono-exponential function of the form[46]

$$I(t) = I_0 + A \quad \exp(-t/\tau)$$

where I_0 is the initial luminescence intensity, τ is the fluorescence decay lifetime, and A represents the constant. The fitted decay curves are presented in Fig. 9(a)–(e). The variation of lifetime with Eu^{3+} concentration follows the same trend as the emission intensity. Specifically, the lifetime increases with Eu^{3+}

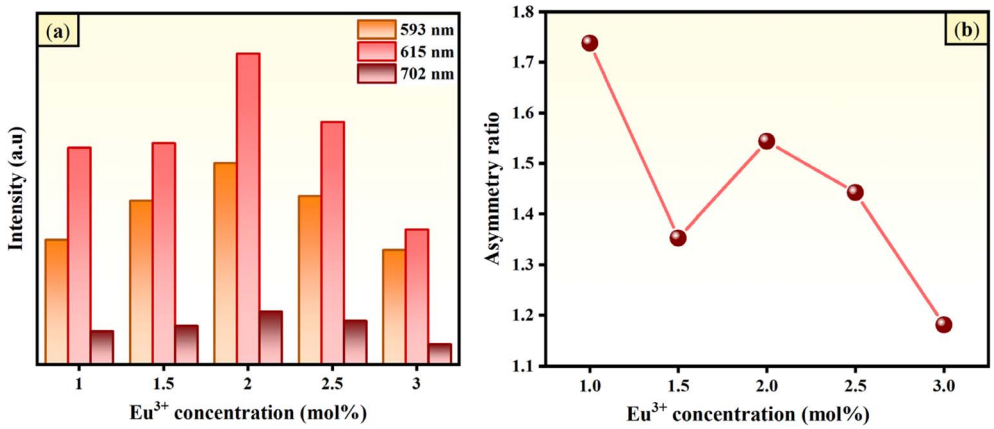

Fig. 7 (a) Variation of intensity for the peaks at 593, 615, and 702 with the concentration of Eu^{3+}. (b) Concentration dependent asymmetry ratio.

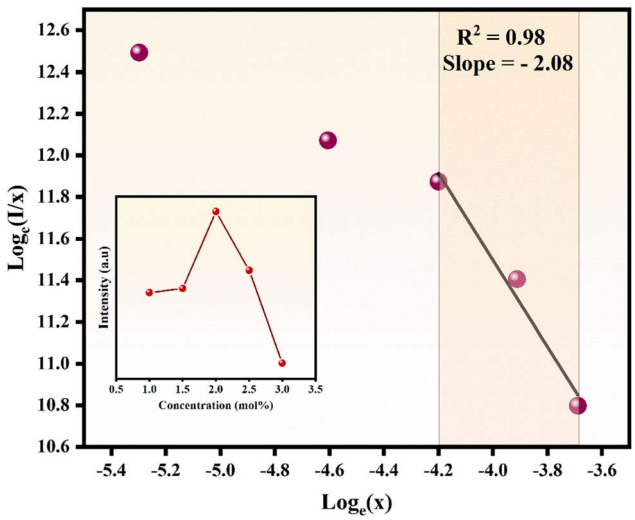

Fig. 8 Dexter plot for the prepared phosphors with variation of PL intensity for 615 nm as the inset.

content and reaches a maximum value of 1.988 ms at 2 mol%, beyond which a progressive decrease is observed. This reduction at higher concentrations is attributed to the enhanced probability of non-radiative energy transfer among closely spaced Eu^{3+} ions, leading to concentration quenching.[47]

3.3 Analysis of colorimetric properties

The emission colour of the phosphors was assessed through colorimetric analysis, employing the Commission Internationale de l'Éclairage (CIE) chromaticity coordinate system to quantitatively assess the perceived colour of the emitted light. The CIE 1931 chromaticity coordinates (x_p, y_p) for all samples were derived from their emission spectra, using an excitation wavelength of 395 nm. The coordinates are summarized in Table 1, and they were found to exhibit minimal variation, indicating consistency in emission colour across different compositions. The CIE coordinates of the prepared phosphors are illustrated in the CIE diagram shown in Fig. 10.[48]

Subsequently, the correlated colour temperature (CCT) was calculated to quantitatively describe the perceived warmth or coolness of the emitted light. Warm white, typically preferred for residential and ambient lighting light is generally characterized by CCT values of below 3200 K, whereas CCT values exceeding 4000 K correspond to cooler light, more suitable for commercial or industrial environments.[49] To estimate the CCT, McCamy's empirical formula was employed[50]

$$CCT = -449n^3 + 3525n^2 - 6823.3n + 5520.33 \quad (6)$$

Here, $n = \frac{x_p - x_0}{y_p - y_0}$ with $(x_0, y_0) = (0.3320, 0.1858)$, representing the chromaticity epicenter of white light convergence. Using the CIE coordinates obtained under 395 nm excitation, the optimal phosphor sample was found to have a CCT value of 1979 K, placing it firmly within the warm light region. The observed variation in CCT values arises from the fact that CCT is calculated based on the chromaticity coordinates (x, y) in the CIE diagram. These coordinates depend on the relative spectral power distribution, that is, the relative intensities of the individual emission peaks. Consequently, even if the overall PL spectrum shape remains largely unchanged, small variations in the relative intensities of peaks can shift the chromaticity coordinates, resulting in changes in the calculated CCT values. The variations in CCT as a function of doping concentration are systematically compiled in Table 1.

Finally, the CIE coordinates were used to compute the colour purity (C P) of the synthesized phosphor materials based on the following standard formula[51]

$$CP = \sqrt{\frac{(x_p - x_0)^2 + (y_p - y_0)^2}{(x_d - x_0)^2 + (y_d - y_0)^2}} \times 100 \quad (7)$$

Here (x_d, y_d) indicates the CIE coordinates for the dominant wavelength on the chromaticity diagram. Using ColorCalculator v7.77 analysis software, and PL data acquired under 395 nm excitation in the 550–750 nm emission range, the CP of all samples was calculated to be nearly 100%. This exceptionally high purity results from the fact that both the sample

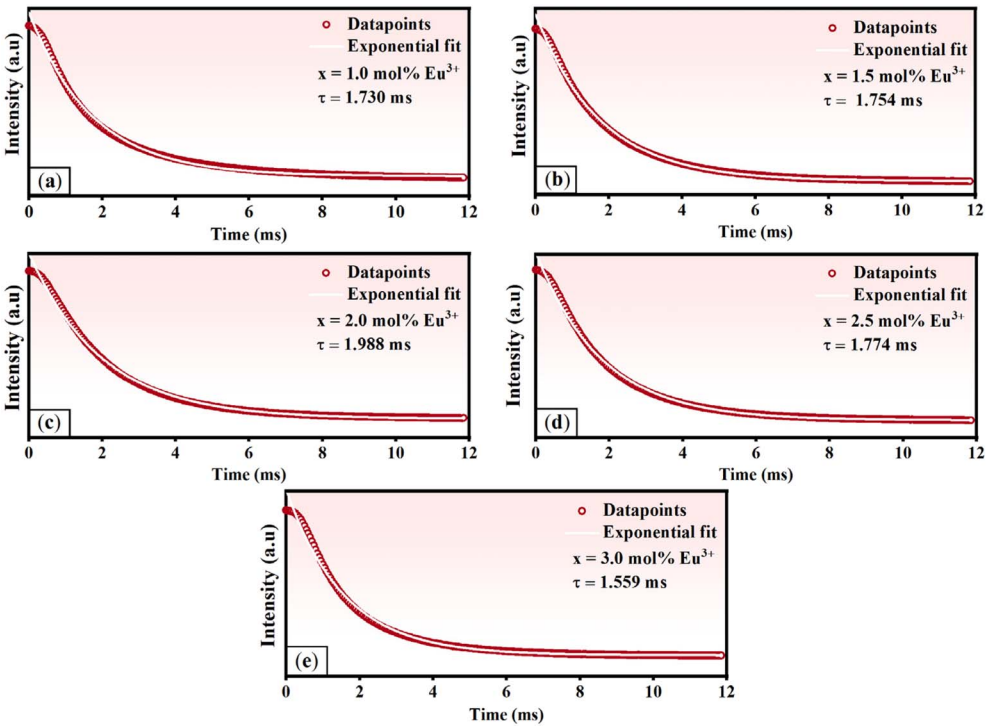

Fig. 9 (a)–(e) Decay curves corresponding to the doped phosphors.

Table 1 CIE 1931 coordinates with CCT and C P for the prepared phosphors

Eu^{3+} (mol%)	x_p	y_p	x_0	y_0	CCT (K)	Colour purity (%)
1.0	0.6376	0.3620	0.3320	0.1858	1948	100
1.5	0.6369	0.3627	0.3320	0.1858	1933	100
2.0	0.6391	0.3606	0.3320	0.1858	1979	100
2.5	0.6352	0.3644	0.3320	0.1858	1900	100
3.0	0.6290	0.3706	0.3320	0.1858	1796	100

coordinates and the dominant wavelength lie nearly coincident at the periphery of the CIE chromaticity diagram. This positioning confirms that the emitted light corresponds to pure reddish-orange emission, with minimal deviation from the dominant wavelength. For clarity, the colorimetric properties are also compared with previously reported phosphors in Table 2, thereby emphasizing the consistency of the observed trends with earlier studies. The evaluation reveals that the β-BaB_2O_4:Eu^{3+} phosphor exhibits notably higher CP relative to its counterparts. This enhanced chromatic performance underscores the material's effectiveness as a high-quality orange-red emitter. As a result, the synthesized phosphor exhibits significant potential as a viable candidate for its potential applicability in warm colour emitting devices.

3.4 Analysis of DRS spectra

The combination of diffuse reflectance spectrum and absorbance spectrum for the β-BaB_2O_4:xEu^{3+} ($x = 2$ mol%) phosphor is presented in Fig. 11. Within the wavelength range of 250 to 350 nm, the spectra show prominent absorption, primarily resulting from CTB transitions between O^{2-} and Eu^{3+} ions, features consistent with those observed in their excitation spectra. Additionally, two weaker absorption peaks are identified near 390 nm and 470 nm, due to the 4f–4f transitions of RE ions.[62]

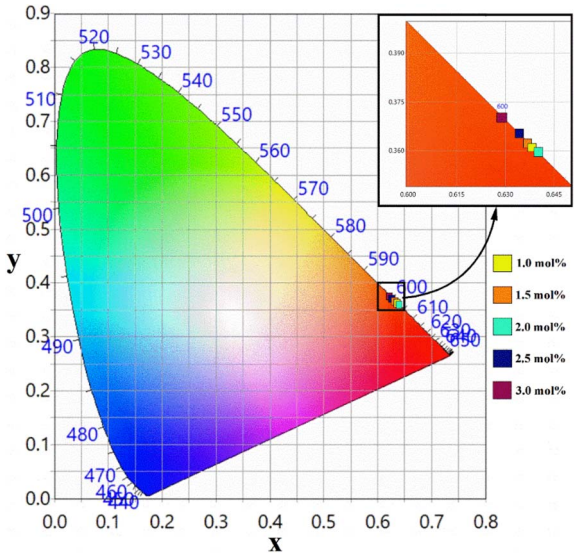

Fig. 10 Chromaticity coordinates of the synthesized phosphors in the CIE 1931 colour coordinate diagram.

Table 2 Comparison of colorimetric parameters of β-BaB_2O_4:xEu^{3+} (x = 2 mol%) phosphor with various previously reported Eu^{3}+ doped phosphors[a]

Phosphor	x_c	(x_p, y_p)	CP (%)	CCT (K)	Ref.
Li_2SiO_3:Eu^{3+}	4 mol%	(0.5800, 0.3375)	75	1240	52
$Ba_3Lu_4O_9$:Eu^{3+}	5 mol%	(0.6535, 0.3461)	95	2710	53
$SrZrO_3$:Eu^{3+}	5 mol%	(0.6262, 0.3333)	92	4324	54
Ba_2LaTaO_6:Eu^{3+}	35 mol%	(0.5872, 0.4064)	98.16	1723	55
Sr_3LiSbO_6:Eu^{3+}	2 mol%	(0.6166, 0.3802)	99.2	1818	56
$Ba_5P_6O_{20}$:Eu^{3+}	12 mol%	(0.6471, 0.3494)	91.4	4336	57
$SrLaGaO_4$:Eu^{3+}	30 mol%	(0.647, 0.353)	99.56	4431	58
$LiYO_2$:Eu^{3+}	20 mol%	(0.662, 0.335)	98.9	4354	59
Na_2ZrO_3:Eu^{3+}	2 mol%	(0.65, 0.35)	91.57	2524	60
$KCaF_3$:Eu^{3+}	6 mol%	(0.5736, 0.4224)	95.56	1565	61
β-BaB_2O_4:Eu^{3+}	2 mol%	(0.6391, 0.3606)	100	1979	This work

[a] x_c = optimized Eu^{3+} concentration.

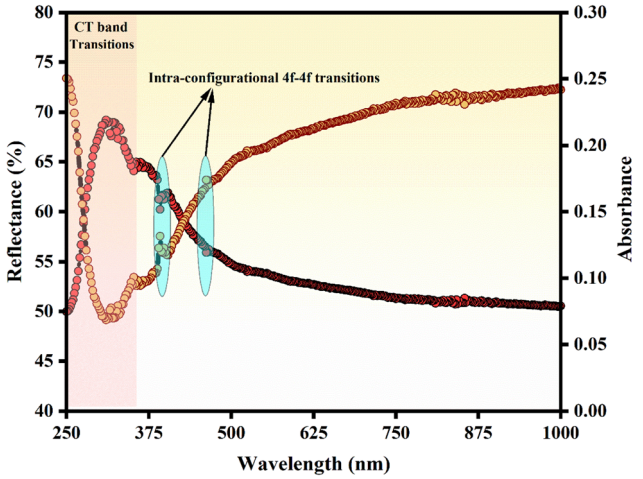

Fig. 11 Absorbance and reflectance spectra in the UV-Vis-NIR range for the optimized phosphor.

Next, the optical band gap (E_g) was calculated by transforming the DRS measurements into the Kubelka–Munk function $F(R)$, as described by the equation below[63]

$$F(R) = \frac{(1-R)^2}{2R} = \frac{\alpha}{S} \quad (8)$$

where α, R, and S denote the absorption coefficient, reflectance, and the scattering coefficient, respectively, with S considered to be a constant across the measured wavelength range.[64] To further evaluate E_g, the Tauc relation was applied, which links α to the photon energy ($h\nu$) as follows[65]

$$\alpha h\nu = C(h\nu - E_g)^n \quad (9)$$

In this equation, C denotes a constant, and the numerical exponent n is equal to 2 for indirect allowed transitions and 1/2 for direct allowed transitions. Given the direct proportionality between α and $F(R)$, the Tauc equation can be rearranged as

$$[F(R)h\nu]^{1/n} = B(h\nu - E_g) \quad (10)$$

with B being the constant of proportionality.

To estimate the band gap value of optimized phosphors, a graph of $[F(R)h\nu]^{1/n}$ and $[F(R)h\nu]^n$against $h\nu$ was plotted. The E_g was then obtained by extrapolating the linear segment of the graph to the photon energy axis. The Tauc's plots corresponding to the optimized sample are shown in Fig. 12(a) and (b). Here, n = 1/2 shows the better linear fit, and hence it can be concluded that the β-BaB_2O_4:xEu^{3+} (x = 2 mol%) phosphor shows a direct band gap, and the E_g value was calculated to be 4.30 eV.

3.5 Analysis of TGA curve

TGA studies were performed to assess the thermal stability of the β-BaB_2O_4:xEu^{3+} (x = 2 mol%) phosphor at elevated temperatures. The obtained TGA curves for both the undoped and Eu^{3+} doped samples, presented in Fig. 13, exhibit an initial weight increase followed by a gradual decrease with rising temperature. The slight initial mass gain is attributed to the adsorption of atmospheric gases on the sample surface, while

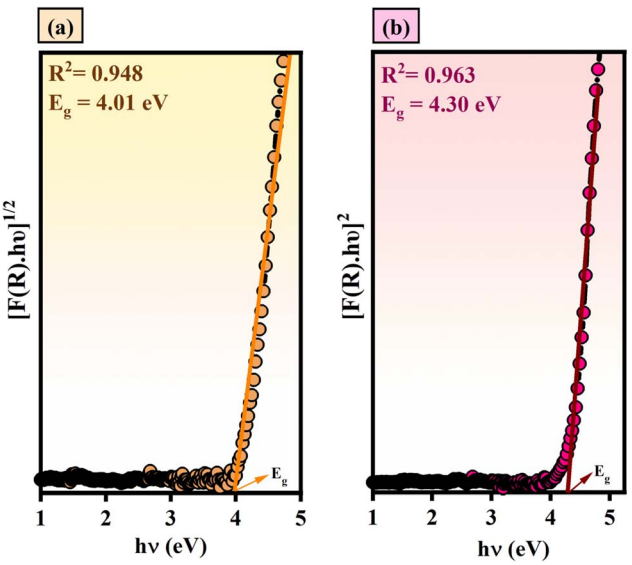

Fig. 12 Tauc plot for the optimized phosphor with (a) n = 2, (b) n = 1/2.

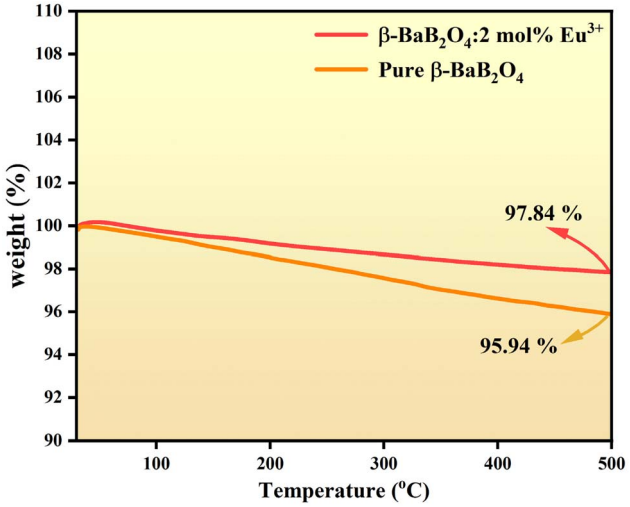

Fig. 13 TGA curve for β-BaB_2O_4:xEu^{3+} (x = 2 mol%) phosphor.

the subsequent weight loss primarily results from the desorption and evaporation of physically adsorbed moisture and residual volatile species.[66] Importantly, no significant mass loss or decomposition event was observed throughout the heating process, indicating the strong thermal robustness of the host lattice. The optimized β-BaB_2O_4:2 mol% Eu^{3+} phosphor retained its structural integrity up to 500 °C, exhibiting only a minor mass loss of about 2.16 wt%, compared to 4.06 wt% for the pure host. This demonstrates that Eu^{3+} incorporation not only enhances the luminescent properties but also slightly improves the thermal stability of the material, confirming its suitability for high-temperature optoelectronic and photonic applications.

3.6 Analysis of JO parameters

To assess the radiative parameters of RE ions in the host matrix, it is important to examine the JO parameters, namely Ω_k (k = 2, 4, 6).[67,68] These parameters also provide valuable information regarding the local symmetry, bonding characteristics, and covalency around the RE ion within the host lattice. Among them, Ω_2 is particularly sensitive to changes in the local symmetry and ligand field, making it a reliable indicator of covalency and the structural configuration around the dopant ion. Meanwhile, Ω_4 and Ω_6 are primarily linked to the macroscopic properties of the host, including rigidity, viscosity, and dielectric behaviour.[69] JO parameters are usually obtained from absorption spectra; however, for Eu^{3+} doped phosphors, the $^5D_0 \rightarrow {}^7F_1$ transition remains largely unaffected by local surroundings and is therefore used as a reliable reference to calculate electric dipole transition probabilities for other transitions. These include transitions $^5D_0 \rightarrow {}^7F_{J'}$ (J' = 2, 4, 6), which are influenced by the local symmetry and are used to extract the JO parameters for the prepared phosphors.[70] In our work, the Ω_6 parameter could not be calculated because the $^5D_0 \rightarrow {}^7F_6$ emission transition was too weak to be observed. As is commonly reported for Eu^{3+} systems, Ω_6 was therefore considered to be zero in the determination of the luminescence radiative properties.[71]

First, we define the spontaneous emission probability of a magnetic dipole[72]

$$A^{md}_{J'-J} = \frac{64\pi^4}{\lambda^3_{md} 3h(2J'+1)} [n^3] S_{md} \quad (11)$$

Similarly, for an electric dipole

$$A^{ed}_{J'-J} = \frac{64\pi^4 e^2}{\lambda^3_{ed} 3h(2J'+1)} \frac{n(n^2+2)^2}{9} \sum_{J=2,4} \Omega_J \left\| \left\langle {}^5D_0 \middle| U^{(J)} {}^5F_J \right\rangle \right\|^2 \quad (12)$$

Here, n represents the refractive index of the host material, while S_{md} is equal to 7.83 × 10^{-42} esu^2 cm^2, corresponding to the magnetic dipole line strength for Eu^{3+} ions, which remains unaffected by the surrounding host matrix.[73] The parameter λ_{md} and λ_{ed} denotes the wavelengths, e is the charge of an electron, h denotes Planck's constant, and $(2J'+1)$ refers to the degeneracy of the excited state. The squared reduced matrix elements $\|\langle {}^5D_0 | U^{(J)} | {}^7F_2 \rangle\|^2$ = 0.0023 and $\|\langle {}^5D_0 | U^{(J)} | {}^7F_4 \rangle\|^2$ = 0.0032, respectively.[74]

First, we take the intensity ratio of emission bands originating from the magnetic dipole (I_{md}) and electric dipole (I_{ed}) transitions can be represented as follows[75]

$$R = \frac{I_{ed}}{I_{md}} = \frac{\lambda_{md}}{\lambda_{ed}} \times \frac{A^{ed}_{J'-J}}{A^{md}_{J'-J}}$$

Substituting for $A^{md}_{J'-J}$ and $A^{ed}_{J'-J}$ from eqn (11) and (12) will give us

$$R = \frac{\lambda_{md}}{\lambda_{ed}} \times \left[\frac{3h(2J'+1)}{64\pi^4 \lambda^3_{ed} n^3 S_{md}}\right] \left[\frac{64\pi^4 \lambda^3_{md} e^2}{3h(2J'+1)} \frac{n(n^2+2)^2}{9}\right] \sum_{J=2,4} \Omega_J \left\| \left\langle {}^5D_0 \middle| U^{(J)} {}^5F_J \right\rangle \right\|^2$$

On simplifying, we get

$$R = \left[\frac{\lambda^4_{md}}{\lambda^4_{ed}}\right] \left[\frac{e^2}{S_{md}}\right] \left[\frac{(n^2+2)^2}{9n^2}\right] \sum_{J=2,4} \Omega_J \left\| \left\langle {}^5D_0 \middle| U^{(J)} {}^5F_J \right\rangle \right\|^2 \quad (13)$$

This ratio can also be expressed as

$$R = \frac{\int I_{ed} d\lambda}{\int I_{md} d\lambda} \quad (14)$$

On comparing eqn (13) and (14), we get

$$\frac{\int I_{ed} d\lambda}{\int I_{md} d\lambda} = \left[\frac{\lambda^4_{md}}{\lambda^4_{ed}}\right] \left[\frac{e^2}{S_{md}}\right] \left[\frac{(n^2+2)^2}{9n^2}\right] \sum_{J=2,4} \Omega_J \left\| \left\langle {}^5D_0 \middle| U^{(J)} {}^5F_J \right\rangle \right\|^2$$

Table 3 Summary of JO intensity parameters calculation for the prepared phosphors

Concentration of Eu^{3+} (mol%)	Ω_2 (10^{-20} cm^2)	Ω_4 (10^{-20} cm^2)	Trend	$\Omega_2 : \Omega_4$
1	2.58	0.76	$\Omega_2 > \Omega_4$	3.40
1.5	2.33	0.74	$\Omega_2 > \Omega_4$	3.14
2	2.32	0.74	$\Omega_2 > \Omega_4$	3.14
2.5	2.06	0.57	$\Omega_2 > \Omega_4$	3.59
3	1.82	0.39	$\Omega_2 > \Omega_4$	4.70

Here, the term on the light hand side denotes that they are under the PL emission peaks, and hence, we get

$$\Omega_2 = \frac{1}{0.0032}\left[\frac{\lambda_{ed}^4}{\lambda_{md}^4}\right]\left[\frac{S_{md}}{e^2}\right]\left[\frac{9n^2}{(n^2+2)^2}\right]\frac{\int I_{ed}\mathrm{d}\lambda}{\int I_{md}\mathrm{d}\lambda} \quad (15)$$

$$\Omega_4 = \frac{1}{0.0023}\left[\frac{\lambda_{md}^4}{\lambda_{ed}^4}\right]\left[\frac{S_{md}}{e^2}\right]\left[\frac{9n^2}{(n^2+2)^2}\right]\frac{\int I_{ed}\mathrm{d}\lambda}{\int I_{md}\mathrm{d}\lambda} \quad (16)$$

Table 3 presents the results of calculations and the ratio Ω_2/Ω_4 for the prepared phosphors. For all the prepared phosphors, JO parameters follow $\Omega_2 > \Omega_4$ trends. This condition reflects the enhanced covalency in the Eu–O bonds, which is most prominent at all the doping levels. The elevated Ω_2 parameter in Table 3 emphasizes the hypersensitive nature of the $^5D_0 \rightarrow {}^7F_2$ transition and implies that Eu^{3+} ions occupy sites with a highly polarizable and asymmetric chemical environment.

Additionally, the observed trend of $\Omega_2 > \Omega_4$ further supports the presence of strong metal–ligand covalency and a non-centrosymmetric environment surrounding the Eu^{3+} ions.[76] Additionally, we have presented the comparison of JO parameters and the trend for $\Omega_2 : \Omega_4$ in Table 4.

3.7 Analysis of radiative parameters

Ω_2 and Ω_4 can be used to estimate key radiative properties of Eu^{3+} doped β-BaB_2O_4 phosphors, including total radiative transition probability (A_T), mean lifetime (τ_{mean}), effective bandwidth ($\Delta\lambda_{eff}$), branching ratio ($\beta_{J'-J}$) and stimulated emission cross-section ($\sigma_{J'-J}$), and for the corresponding emission transitions.

For the ith transition, the radiative transition probability[86]

$$A^i_{J'-J} = A^{md}_{J'-J} + A^{ed}_{J'-J}$$

Table 4 Comparison of JO parameters of the optimized phosphor with the previously reported works

Phosphor	Ω_2 (10^{-20} cm^2)	Ω_4 (10^{-20} cm^2)	Ω_4 (10^{-20} cm^2)	Trend	$\frac{\Omega_2}{\Omega_4}$	Ref.
$KBaScSi_3O_9:Eu^{3+}$	1.25	0.38	0	$\Omega_2 > \Omega_4 > \Omega_6$	3.29	77
$CaMoO_4:Eu^{3+}$	11.50	2.65	0	$\Omega_2 > \Omega_4 > \Omega_6$	4.34	78
$Ca_2MgSi_2O_7:Eu^{3+}$	2.80	2.77	0	$\Omega_2 > \Omega_4 > \Omega_6$	1.01	79
$CaZrO_3:Eu^{3+}$	4.36	0.89	0	$\Omega_2 > \Omega_4 > \Omega_6$	4.90	80
$Ba_2GdSbO_6:Eu^{3+}$	1.52	0.53	0	$\Omega_2 > \Omega_4 > \Omega_6$	2.87	81
$Y_2Si_2O_7:Eu^{3+}$	5.91	0.98	0	$\Omega_2 > \Omega_4 > \Omega_6$	6.03	82
$Na_2ZrO_3:Eu^{3+}$	5.12	1.59	0	$\Omega_2 > \Omega_4 > \Omega_6$	3.25	83
$CaGeO_3:Eu^{3+}$	4.59	1.70	0	$\Omega_2 > \Omega_4 > \Omega_6$	2.70	84
$Y_7O_6F_9:Eu^{3+}$	5.70	1.80	0	$\Omega_2 > \Omega_4 > \Omega_6$	3.17	85
β-$BaB_2O_4:Eu^{3+}$	2.32	0.74	0	$\Omega_2 > \Omega_4 > \Omega_6$	3.14	This work

Table 5 Radiative parameters of the prepared phosphors

Eu^{3+} concentration	Transition	$A^{md}_{J'-J}$ (s^{-1})	$A^{ed}_{J'-J}$ (s^{-1})	A_T (s^{-1})	τ_{mean} (s)	β	$\Delta\lambda_{eff}$ (nm)	$\sigma_{J'-J}$ (10^{-23} cm^2)
1 mol%	$^5D_0 \rightarrow {}^7F_2$	—	48.40	88.09	0.0114	0.55	14.80	3.25
	$^5D_0 \rightarrow {}^7F_4$	—	3.82			0.04	11.69	5.51
	$^5D_0 \rightarrow {}^7F_1$	35.87	—			0.41	11.61	2.24
1.5 mol%	$^5D_0 \rightarrow {}^7F_2$	—	43.76	83.37	0.0120	0.52	15.95	2.73
	$^5D_0 \rightarrow {}^7F_4$	—	3.74			0.04	11.61	5.44
	$^5D_0 \rightarrow {}^7F_1$	35.87	—			0.43	10.64	2.90
2 mol%	$^5D_0 \rightarrow {}^7F_2$	—	43.51	83.10	0.0120	0.52	15.15	2.85
	$^5D_0 \rightarrow {}^7F_4$	—	3.72			0.04	11.48	5.47
	$^5D_0 \rightarrow {}^7F_1$	35.87	—			0.43	11.25	2.74
2.5 mol%	$^5D_0 \rightarrow {}^7F_2$	—	38.69	77.45	0.0129	0.50	14.57	2.64
	$^5D_0 \rightarrow {}^7F_4$	—	2.89			0.04	9.99	4.88
	$^5D_0 \rightarrow {}^7F_1$	35.87	—			0.46	11.73	2.63
3 mol%	$^5D_0 \rightarrow {}^7F_2$	—	34.10	71.92	0.0139	0.47	14.83	2.29
	$^5D_0 \rightarrow {}^7F_4$	—	1.95			0.03	9.91	3.32
	$^5D_0 \rightarrow {}^7F_1$	35.87	—			0.50	11.37	2.71

Therefore, the total radiative transition probability is given by

$$A_T = \sum A^i_{J'-J} \quad (17)$$

Using the A_T, we can determine the mean lifetime and branching ratio for a given transition using equations[87]

$$\tau_{mean} = \frac{1}{A_T} \quad (18)$$

$$\beta_{J'-J} = \frac{A^i_{J'-J}}{A_T} \quad (19)$$

Finally, the cross-section of stimulated emission is calculated using[88]

$$\sigma_{J'-J} = \frac{A^i_{J'-J}\lambda^4_{J'-J}}{8\pi cn^2\Delta\lambda_{eff}} \quad (20)$$

where, $\Delta\lambda_{eff}$, c, $A^i_{J'-J}$, and $\lambda_{J'-J}$, represents the FWHM of the emission peak, speed of light, radiative transition probability, and the peak emission wavelength, respectively. Table 5 represents the radiative parameters corresponding to the prepared phosphors. For efficient laser performance, it is preferable for the emission peak to exhibit a narrow FWHM, as this enhances $\sigma_{J'-J}$. A high $\sigma_{J'-J}$ value associated with a strong emission transition is particularly advantageous for applications requiring low lasing thresholds and high optical gain, making the material suitable for laser-based technologies.[89]

In our case, we observe that the branching ratio associated with the $^5D_0 \rightarrow {}^7F_2$ transition is significantly greater than that of the $^5D_0 \rightarrow {}^7F_1$ and $^5D_0 \rightarrow {}^7F_4$ transitions, indicating enhanced colour purity in the studied phosphor material. Furthermore, the elevated values of $\sigma_{J'-J}$ highlight the strong radiative characteristics of the phosphor, making it a promising candidate for laser applications.

4 Conclusions

Eu^{3+} doped β-BaB_2O_4 phosphors were successfully synthesized *via* the solid-state reaction route, and their structural, optical, and thermal properties were systematically investigated. XRD analysis confirmed the formation of a single-phase β-BaB_2O_4 structure without any secondary peaks or lattice distortions, indicating the effective incorporation of Eu^{3+} ions into the host lattice without altering its crystal symmetry. Under 395 nm excitation, the photoluminescence spectra revealed dominant emission bands centered at 581, 593, 615, 653, and 702 nm, corresponding to the $^5D_0 \rightarrow {}^7F_0$, $^5D_0 \rightarrow {}^7F_1$, $^5D_0 \rightarrow {}^7F_2$, $^5D_0 \rightarrow {}^7F_3$, and $^5D_0 \rightarrow {}^7F_4$ transitions, respectively, exhibiting excellent colour purity (≈100%). The concentration quenching behaviour was attributed to non-radiative energy transfer *via* dipole–dipole interactions among adjacent Eu^{3+} ions. The material exhibited a direct band gap of 4.30 eV and exceptional thermal stability, retaining structural integrity with only ~2.18% mass loss at 500 °C. Judd–Ofelt analysis indicated $\Omega_2 > \Omega_4$ for all Eu^{3+} concentrations, implying strong covalent bonding between the Eu^{3+} ions and the host lattice. Furthermore, the asymmetry ratio greater than unity confirmed that Eu^{3+} ions occupy low-symmetry sites within the β-BaB_2O_4 matrix. Among the observed transitions, the $^5D_0 \rightarrow {}^7F_2$ transition exhibited the highest branching ratio and radiative probability, signifying its dominance in the red emission region. Collectively, these findings demonstrate that β-BaB_2O_4:Eu^{3+} phosphors possess superior structural stability, efficient red emission, and favorable electronic characteristics, making them promising candidates for advanced solid-state lighting and laser applications.

Conflicts of interest

There are no conflicts of interest to declare.

Data availability

The data sets generated and/or analyzed in this study are available from the corresponding author on reasonable request.

Acknowledgements

The authors acknowledge the financial support from the Manipal Academy of Higher Education, Manipal, India. The authors express their gratitude to Princess Nourah Bint Abdulrahman University Researchers Supporting Project number (PNURSP2025R2), Princess Nourah Bint Abdulrahman University, Riyadh, Saudi Arabia.

References

1 Y. Tao, C. D. Rahn, L. A. Archer and F. You, *Sci. Adv.*, 2021, **7**, eabi7633.
2 R. Yadav, M. Singh, D. Shekhawat, S.-Y. Lee and S.-J. Park, *Compos. Appl. Sci. Manuf.*, 2023, **175**, 107775.
3 F. Khan, N. Hossain, J. J. Mim, S. M. Rahman, Md. J. Iqbal, M. Billah and M. A. Chowdhury, *J. Eng. Res.*, 2025, **13**, 1001–1023.
4 Q. Shi, J. Zhou, S. Ullah, X. Yang, K. Tokarska, B. Trzebicka, H. Q. Ta and M. H. Rümmeli, *Energy Storage Mater.*, 2021, **34**, 735–754.
5 J. Zhang, D. Shao, L. Jiang, G. Zhang, H. Wu, R. Day and W. Jiang, *Renew. Sustain. Energy Rev.*, 2022, **159**, 112207.
6 R. Aksakal, C. Mertens, M. Soete, N. Badi and F. Du Prez, *Adv. Sci.*, 2021, **8**, 2004038.
7 V. Erduran, M. Bekmezci, R. Bayat and F. Sen, in *Functionalized Nanomaterial-Based Electrochemical Sensors*, Elsevier, 2022, pp. 97–111.
8 A. Dwivedi, A. Roy and S. B. Rai, *RSC Adv.*, 2023, **13**, 16260–16271.
9 R. Mahajan and R. Prakash, *J. Mater. Sci.: Mater. Electron.*, 2022, **33**, 25491–25517.
10 D. K. Patel and V. K. Sharma, *Trans. Indian Inst. Met.*, 2025, **78**, 165.
11 R. Kiran, N. Kamath, M. I. Sayyed, A. H. Almuqrin and S. D. Kamath, *RSC Adv.*, 2025, **15**, 20040–20060.
12 M. M. Lanje, M. M. Yawalkar, J. S. Dahegaonkar and S. J. Dhoble, *J. Phys.: Conf. Ser.*, 2021, **1913**, 012031.

13 P. K. Tawalare, *Luminescence*, 2022, **37**, 1226–1245.
14 A. N. Yerpude and S. J. Dhoble, in *Phosphor Handbook*, Elsevier, 2023, pp. 155–176.
15 K. R, P. A, S. M. M. Kennedy, M. I. Sayyed, T. A. Hanafy, V. Mishra and S. D. Kamath, *J. Mol. Struct.*, 2025, **1322**, 140381.
16 R. Kiran, H. M. Pratheeksha, V. Saraswathi A, A. Princy, S. M. M. Kennedy, A. S. Altowyan, M. I. Sayyed and S. D. Kamath, *J. Solid State Chem.*, 2024, **337**, 124792.
17 L. H. A. R. Ferreira, G. Dantelle, A. Ibanez and L. J. Q. Maia, *Phys. B*, 2022, **644**, 414193.
18 W. G. Zou, M. K. Lü, F. Gu, S. Wang, Z. Xiu and G. Zhou, *Mater. Sci. Eng. B*, 2006, **127**, 134–137.
19 J. Lakde, C. M. Mehare, K. K. Pandey, N. S. Dhoble and S. J. Dhoble, *J. Phys.: Conf. Ser.*, 2021, **1913**, 012029.
20 R. S. Yadav and S. B. Rai, *J. Phys. Chem. Solids*, 2017, **110**, 211–217.
21 S. Yadav, D. Kumar, R. S. Yadav, S. B. Rai and A. K. Singh, *Ceram. Int.*, 2022, **48**, 30754–30766.
22 Monika, R. S. Yadav, A. Bahadur and S. B. Rai, *RSC Adv.*, 2023, **13**, 20164–20178.
23 E. Rai, R. S. Yadav, D. Kumar, A. K. Singh, V. J. Fulari and S. B. Rai, *RSC Adv.*, 2023, **13**, 4182–4194.
24 J. Liu, X.-D. Wang, Z.-C. Wu and S.-P. Kuang, *Spectrochim. Acta Mol. Biomol. Spectrosc.*, 2011, **79**, 1520–1523.
25 Z. Li, H. Ma, N. Li, Y. Du and Q. Shao, *J. Alloys Compd.*, 2018, **747**, 340–347.
26 R. S. Yadav and S. B. Rai, *J. Alloys Compd.*, 2017, **700**, 228–237.
27 E. Rai, R. S. Yadav, D. Kumar, A. K. Singh, V. J. Fulari and S. B. Rai, *J. Lumin.*, 2022, **241**, 118519.
28 P. Du, X. Huang and J. S. Yu, *Inorg. Chem. Front.*, 2017, **4**, 1987–1995.
29 X. Tian, L. Guo, J. Wen, L. Zhu, C. Ji, Z. Huang, H. Qiu, F. Luo, X. Liu, J. Li, C. Li, Y. Peng, J. Cao, Z. He and H. Zhong, *J. Alloys Compd.*, 2023, **959**, 170574.
30 A. Khorsand Zak, W. H. A. Majid, M. E. Abrishami and R. Yousefi, *Solid State Sci.*, 2011, **13**, 251–256.
31 P. Rohilla and A. S. Rao, *Mater. Res. Bull.*, 2022, **150**, 111753.
32 K. Ganesh Kumar, P. Balaji Bhargav, K. Aravinth, N. Ahmed and C. Balaji, *Ceram. Int.*, 2022, **48**, 36038–36045.
33 E. Rai, R. S. Yadav, D. Kumar, A. K. Singh, V. J. Fulari and S. B. Rai, *J. Lumin.*, 2022, **241**, 118519.
34 Q. Zhao, J. Chen, X. Jing, T. Lang, M. Cai, L. Peng, Q. Qiang, W. Chen, E. F. Polisadova and B. Liu, *J. Lumin.*, 2024, **276**, 120878.
35 W. T. Carnall, P. R. Fields and K. Rajnak, *J. Chem. Phys.*, 1968, **49**, 4450–4455.
36 C. Hernández-Fuentes, R. Ruiz-Guerrero, A. Morales-Ramírez, P. Molina-Maldonado and D. Medina-Velazquez, *Crystals*, 2020, **10**, 674.
37 A. Hooda, S. P. Khatkar, A. Khatkar, R. K. Malik, S. Devi, J. Dalal and V. B. Taxak, *J. Mater. Sci.: Mater. Electron.*, 2019, **30**, 8751–8762.
38 N. Degda, N. Patel, V. Verma, K. V. R. Murthy, N. Chauhan, M. Singhal and M. Srinivas, *Opt. Mater.*, 2023, **142**, 114019.
39 V. Ghenea, I. Culeac and A. Buzdugan, *J. Eng. Sci.*, 2024, **31**, 28–38.
40 P. J. Chaware, Y. D. Choudhari, D. M. Borikar and K. G. Rewatkar, *Opt. Mater.*, 2022, **133**, 112945.
41 Y. Du, Y. Li, Y. Zhao, X. Zhang, C. Li, R. Yang, Z. Zou, J. Lian, J. Duan, H. Lin and R. Yu, *J. Lumin.*, 2023, **260**, 119893.
42 Q. Lv, R. Deng, J. Guo, Z. Zhou, Z. Ma, X. Hu, W. Shi, B. Deng, Y. Yu and R. Yu, *J. Lumin.*, 2022, **252**, 119320.
43 D. L. Dexter, *J. Chem. Phys.*, 1953, **21**, 836–850.
44 S. Kaur, A. S. Rao and M. Jayasimhadri, *Ceram. Int.*, 2017, **43**, 7401–7407.
45 T. A. Safeera and E. I. Anila, *J. Lumin.*, 2019, **205**, 277–281.
46 P. Du, J. Tang, W. Li, L. Luo and M. Runowski, *Mater. Today Chem.*, 2022, **26**, 101013.
47 H. Li, J. Zhu, Z. Fang, X. Xiang, J. Jiao, H. Zhang, W. Hu and J. Zhu, *Mater. Today Chem.*, 2023, **30**, 101558.
48 Y. Ma, S. Tang, C. Ji, D. Wu, S. Li, J. Xu, T. Zeng, Z. Huang, H. He and Y. Peng, *J. Lumin.*, 2022, **242**, 118530.
49 B. Das, S. Bardhan, T. Maity and S. Mazumdar, *Results Opt.*, 2020, **1**, 100013.
50 C. S. McCamy, *Color Res. Appl.*, 1992, **17**, 142–144.
51 H. Gao, J. Zhao, Y. Zhang, X. Zhang, H. Bu, Z. Zhao, X. Song, Z. Yang and J. Sun, *J. Appl. Phys.*, 2021, **129**, 143102.
52 P. Barik, A. Verma, R. Kumar, V. Kumar and I. P. Sahu, *Appl. Phys. A*, 2023, **129**, 677.
53 A. Khatkar, D. Kumar, R. Kumar and S. Lata, *J. Fluoresc.*, 2025, DOI: **10.1007/s10895-025-04338-3**.
54 K. C. Sushma, R. B. Basavaraj, D. P. Aarti, M. B. M. Reddy, G. Nagaraju, M. S. Rudresha, H. M. S. Kumar and K. N. Venkatachalaiah, *J. Mol. Struct.*, 2023, **1283**, 135192.
55 F. Li, R. Cui, G. Yuan, X. Zhang, M. Zhang and C. Deng, *J. Rare Earths*, 2023, **41**, 1678–1688.
56 C. Kumari, J. Manam and S. K. Sharma, *Mater. Sci. Semicond. Process.*, 2023, **158**, 107385.
57 Z. Guo, H. Jiang, H. Li, H. Zhang, C. Liu, R. Zhao, Z. Yang, H. Tang, J. Li, J. Zhang and J. Zhu, *Appl. Mater. Today*, 2024, **37**, 102095.
58 Y. Qiu, R. Cui, J. Zhang and C. Deng, *J. Solid State Chem.*, 2023, **327**, 124265.
59 L. Zhang, Y. Xu, X. Wu, S. Yin and H. You, *Mater. Adv.*, 2022, **3**, 2591–2597.
60 P. Khajuria, V. D. Sharma, I. Kumar, A. Khajuria, R. Prakash and R. J. Choudhary, *J. Alloys Compd.*, 2025, **1025**, 180268.
61 R. Kameshwaran, A. Raja, R. R. Kumar, D. J. Daniel, D. O. Annalakshmi, K. Aravinth, P. B. Bhargav and P. Ramasamy, *Appl. Radiat. Isot.*, 2023, **191**, 110520.
62 S. Verma, I. Ayoub, S. Som, V. Sharma, G. Kumar, H. C. Swart and V. Kumar, *Opt. Mater.*, 2023, **136**, 113416.
63 A. A. Christy, O. M. Kvalheim and R. A. Velapoldi, *Vib. Spectrosc.*, 1995, **9**, 19–27.
64 L. F. Gate, *Appl. Opt.*, 1974, **13**, 236.
65 Anu and A. S. Rao, *Opt. Mater.*, 2023, **145**, 114476.
66 N. S. Bajaj and S. K. Omanwar, *J. Lumin.*, 2014, **148**, 169–173.
67 B. R. Judd, *Phys. Rev.*, 1962, **127**, 750–761.
68 G. S. Ofelt, *J. Chem. Phys.*, 1962, **37**, 511–520.
69 B. Verma, R. N. Baghel, D. P. Bisen, N. Brahme and V. Jena, *Opt. Mater.*, 2022, **123**, 111787.

70 A. Ćirić, S. Stojadinović, M. Sekulić and M. D. Dramićanin, *J. Lumin.*, 2019, **205**, 351–356.
71 Q. Chen, B. Miao, P. S. Kumar and S. Xu, *Opt. Mater.*, 2021, **116**, 111093.
72 S. R. Yashodha, N. Dhananjaya, S. R. Manohara and H. S. Yogananda, *J. Mater. Sci.: Mater. Electron.*, 2021, **32**, 11511–11523.
73 W. F. Krupke, *Phys. Rev.*, 1966, **145**, 325–337.
74 W. T. Carnall, P. R. Fields and K. Rajnak, *J. Chem. Phys.*, 1968, **49**, 4450–4455.
75 R. Venkatesh, N. Dhananjaya, M. K. Sateesh, J. P. Shabaaz Begum, S. R. Yashodha, H. Nagabhushana and C. Shivakumara, *J. Alloys Compd.*, 2018, **732**, 725–739.
76 S. Tanabe, T. Ohyagi, N. Soga and T. Hanada, *Phys. Rev. B: Condens. Matter Mater. Phys.*, 1992, **46**, 3305–3310.
77 R. Nagaraj, A. Raja and S. Ranjith, *J. Alloys Compd.*, 2020, **827**, 154289.
78 H. N. Van, M. T. Yen Thanh, V.-H. Pham, P. Van Huan, V. T. Ngoc Minh, P. A. Tuan and H. T. Duy, *Opt. Mater.*, 2022, **132**, 112831.
79 P. J. Chaware, Y. D. Choudhari, D. M. Borikar and K. G. Rewatkar, *Opt. Mater.*, 2022, **133**, 112945.
80 S. Jang, J. Lee, S. W. Wi, H. Lim, Y. J. Jeong, J.-S. Chung, W. K. Kang and Y. S. Lee, *J. Lumin.*, 2021, **240**, 118433.
81 C. Kumari, J. Manam and S. K. Sharma, *J. Lumin.*, 2023, **263**, 119983.
82 P. Kumar, D. Singh, S. Kadyan, H. Kumar and R. Kumar, *Ceram. Int.*, 2024, **50**, 34596–34608.
83 P. Khajuria, V. D. Sharma, I. Kumar, A. Khajuria, R. Prakash and R. J. Choudhary, *J. Alloys Compd.*, 2025, **1025**, 180268.
84 W. Hu, Y. Jin, Y. Chen, Y. Wei, C. Wang, Z. Zhang, F. Meng and H. Ren, *J. Alloys Compd.*, 2024, **1008**, 176702.
85 N. Rakov, F. Matias and G. S. Maciel, *Phys. B*, 2023, **652**, 414625.
86 H. N. Van, M. T. Yen Thanh, V.-H. Pham, P. Van Huan, V. T. Ngoc Minh, P. A. Tuan and H. T. Duy, *Opt. Mater.*, 2022, **132**, 112831.
87 S. S. Babu, P. Babu, C. K. Jayasankar, W. Sievers, Th. Tröster and G. Wortmann, *J. Lumin.*, 2007, **126**, 109–120.
88 S. B. Mallur, T. C. Khoo, S. Rijal, O. R. Huff and P. K. Babu, *Mater. Chem. Phys.*, 2021, **258**, 123886.
89 T. Krishnapriya, A. Jose, T. A. Jose, E. Sreeja, N. V. Unnikrishnan and P. R. Biju, *J. Mater. Sci.: Mater. Electron.*, 2020, **31**, 22452–22466.